https://doi.org/10.5194/egusphere-2024-571
Preprint. Discussion started: 26 March 2024

Calving of Ross Ice Shelf from wave erosion and hydrostatic stresses

Nicolas B. Sartore[1], Till J.W. Wagner[1], Matthew R. Siegfried[2], Nimish Pujara[3], and Lucas K. Zoet[4]

[1]Department of Atmospheric and Oceanic Sciences, University of Wisconsin-Madison, Madison, USA
[2]Department of Geophysics, Colorado School of Mines, Golden, USA
[3]Department of Civil and Environmental Engineering, University of Wisconsin-Madison, Madison, USA
[4]Department of Geoscience, University of Wisconsin-Madison, Madison, USA

Correspondence: Nicolas B. Sartore (nsartore@wisc.edu) and Till J.W. Wagner (till.wagner@wisc.edu)

Abstract. Ice shelf calving constitutes roughly half of the total mass loss from the Antarctic ice sheet. Although much attention is paid to calving of giant tabular icebergs, these events are relatively rare. More frequent, smaller-scale calving events likely play an important role in the ice shelf frontal dynamics. Here, we investigate the role of bending stresses at the ice shelf front in driving calving on the scale 100 m – 1 km, perpendicular to the ice edge. We focus in particular on how buoyant underwater "feet" that protrude beyond the above-water ice cliff may cause tensile stresses at the base of the ice and ultimately lead to fracture. Indirect and anecdotal observations of such feet at the Ross Ice Shelf front suggest that this process may be widespread. We consider satellite observations, together with an elastic beam model and a parameterization of frontal wave erosion to estimate the size and frequency of such calving events. Our results suggest that foot-induced mass loss at Ross Ice Shelf may cause up to 25% of the total frontal ablation. However, stresses induced through this process are likely not sufficient to initiate crevassing but rather act to propagate existing crevasses. In addition, the relatively strong ice thickness dependence of the frontal uplift suggests an important role for internal bending moments due to temperature gradients in the ice. The highly variable environment, irregularity of pre-existing crevasse spacing, and complex rheology of the ice continue to pose challenges in better constraining the drivers behind the observed deformations and resulting calving rates.

1 Introduction

High-emission climate model scenarios project that likely mass loss from the Antarctic ice sheet may raise global mean sea level by up to 45 cm by 2100, relative to the 1994–2014 average (Pattyn and Morlighem, 2020; Seroussi et al., 2020; Fox-Kemper et al., 2021). Beyond sea-level rise, the associated meltwater input alters the temperature and stratification of the Southern Ocean with impacts on the global climate (e.g., Golledge et al., 2019; Jeong et al., 2020; Li et al., 2023). These increases in melt represent a sufficiently substantial modification of the Southern Ocean system that they should be included as a historical forcing in climate simulations (Schmidt et al., 2023).

Antarctic ice mass loss occurs mainly through the ablation of ice shelves, which is dominated by two processes: basal melting and calving. For the two largest ice shelves, Ross and Filchner-Ronne, calving is assessed to be responsible for at least 50% of the mass loss, reaching close to 100% for the Western Ross Ice Shelf (Rignot et al., 2013; Greene et al., 2022).

https://doi.org/10.5194/egusphere-2024-571
Preprint. Discussion started: 26 March 2024

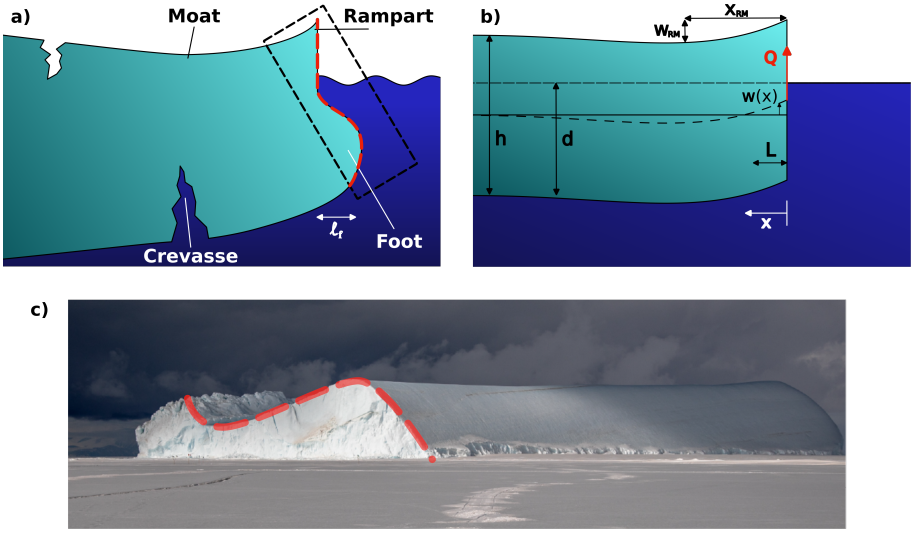

Figure 1. Foot-induced deformation of an ice shelf front. (a) Diagram of an ice shelf front deflected by an underwater buoyant foot of cross-edge dimension l_f, leading to basal crevasse propagation (not to scale). (b) Elastic beam approximation, where w (dashed curve) is the ice shelf center-line profile relative to the undeflected shelf (solid line), Q is a point force applied at the front, representing the net upward buoyant force exerted by the foot, L is the calving size computed from the point of maximum stress. In reality, L would be determined by a complex interplay between crevassing and the applied stresses. (c) Photo taken in 2019 by Justin Lawrence (used with permission) of an iceberg that calved off western Ross Ice Shelf near 166° E and was subsequently frozen into sea ice. The iceberg likely rotated after calving due to the excess buoyancy of the foot, leading to the smooth and previously submerged part of the ice cliff to be visible. This part exhibits a foot (with l_f several tens of meters) beneath the more rugged above-water ice cliff. The approximate visible part is indicated as a rectangle in panel a and the corresponding frontal profiles in panels a and c are indicated by the red dashed line. The horizontal along-front width of the iceberg is roughly 500 m.

Ice shelf calving has received substantial attention in recent years, with great advances in theoretical, modeling, and observational approaches (see reviews by Benn et al., 2017; Alley et al., 2023). Modes of calving range from frequent small-scale failure of the above-water ice cliff to sporadic detachments of giant tabular icebergs. Here, we focus on intermediate-scale processes that have received less attention: calving due to bending stresses in the ice. The role of bending was recently studied for the ice shelf interior in driving crevasse opening (Buck and Lai, 2021). However, bending is also encountered at ice fronts when melting is not uniform with depth, leading to undercutting or overcutting of the ice cliff. The resulting hydrostatic imbalance leads to bending stresses in the ice and flexure that can cause calving events much larger than the loss due to frontal melt alone. This has been termed the calving-multiplier effect (e.g., Slater et al., 2021).

Depth variations in frontal melt can result from several processes, such as enhanced basal melt due to a subglacial discharge plume (Jenkins, 2011) or increased near-waterline melt due to advection of warmer surface waters (Slater et al., 2018). Here, we focus on ocean surface waves as a primary driver of non-uniform melting, and thereby non-uniform erosion. When the cliff of an ice shelf is exposed to open water, waves melt a notch at the calving front, which over time leads to the gravity-driven

https://doi.org/10.5194/egusphere-2024-571
Preprint. Discussion started: 26 March 2024

collapse of the overhanging ice slab. The submerged front of the ice shelf then protrudes beyond the above-water cliff and is no longer in hydrostatic equilibrium. The excess buoyancy of this protrusion, or foot, will cause the front of the ice shelf to bend upward. This bending results in a characteristic surface deformation that Scambos et al. (2005) termed a rampart–moat profile (Figure 1). These wave-induced erosion steps repeat several times until the tensile stress due to buoyancy-induced bending exceeds the strength of the ice, triggering a calving event. This calving process has been referred to as the "footloose" mechanism (Wagner et al., 2014).

Observing the underwater section of tidewater glaciers and ice shelves is often hazardous and little direct data was available until recently. However, new technological advances such as the use of uncrewed vehicles have demonstrated that submerged feet or, more generally, overcutting is a widespread phenomenon (e.g., Sutherland et al., 2019; Abib et al., 2023). The rampart–moat surface expression of a buoyant foot is more readily observed than the foot itself. For example, James et al. (2014) observed the progression of a rampart–moat profile at Helheim Glacier before and after a calving event. Wagner et al. (2016) argued that this deformation may be explained by a growing submerged foot. Rampart–moat profiles have also been observed for icebergs, e.g., from ICESat data (Scambos et al., 2005) or ship-based lidar (Wagner et al., 2014). The latter study also revealed direct observations of a coinciding foot (using multi-beam sonar for underwater imagery that was paired with the above-water lidar). Since in many cases only the rampart–moat surface profile is observed, the presence of a foot tends to be indirectly inferred, and other possible drivers of the surface deformation exist. One alternative driver are internal stresses that result from strong temperature gradients in the ice shelf, a process recently explored by Buck (2024). Part of the motivation of the present study is to explore whether the characteristic bending due to a foot together with estimated wave-notch melt rates is consistent with recent observations of rampart–moat profiles and calving events at Ross Ice Shelf.

While the role of footloose-type calving has been studied for tabular icebergs (e.g., England et al., 2020; Huth et al., 2022) and tidewater glaciers (e.g., Trevers et al., 2019), its potential impact on Antarctic ice shelves has not been investigated in detail. However, a recent analysis of satellite altimetry data from NASA's Ice, Cloud, and land Elevation Satellite 2 (ICESat-2) mission by Becker et al. (2021) shows that much of the Ross Ice Shelf front exhibits conspicuous rampart–moat profiles, suggesting that the footloose mechanism may be prevalent for much of Ross Ice Shelf and potentially other ice shelves.

In this study, we use satellite data of the ice shelf elevation as motivating observations to explore the role of footloose-type calving at Ross Ice Shelf. First, we compare the observed profiles with solutions of an idealized elastic beam representation of the ice shelf. Second, we estimate the foot growth rates using a parameterization of wave erosion at the ice front. Finally, we combine these results to assess the potential calving rate and volume at Ross Ice Shelf due to foot-induced flexure.

2 Motivating observations of Ross Ice Shelf surface profiles from ICESat and ICESat-2

The underwater section of the Ross Ice Shelf calving front has not been observed in situ, making it challenging to directly verify the existence or shape of an underwater foot. The photo in Figure 1c of an iceberg that capsized after calving, revealing the distinct profile of an underwater foot presents a rare exception and provides perhaps the strongest existing direct evidence of such a foot at Ross Ice Shelf.

https://doi.org/10.5194/egusphere-2024-571
Preprint. Discussion started: 26 March 2024

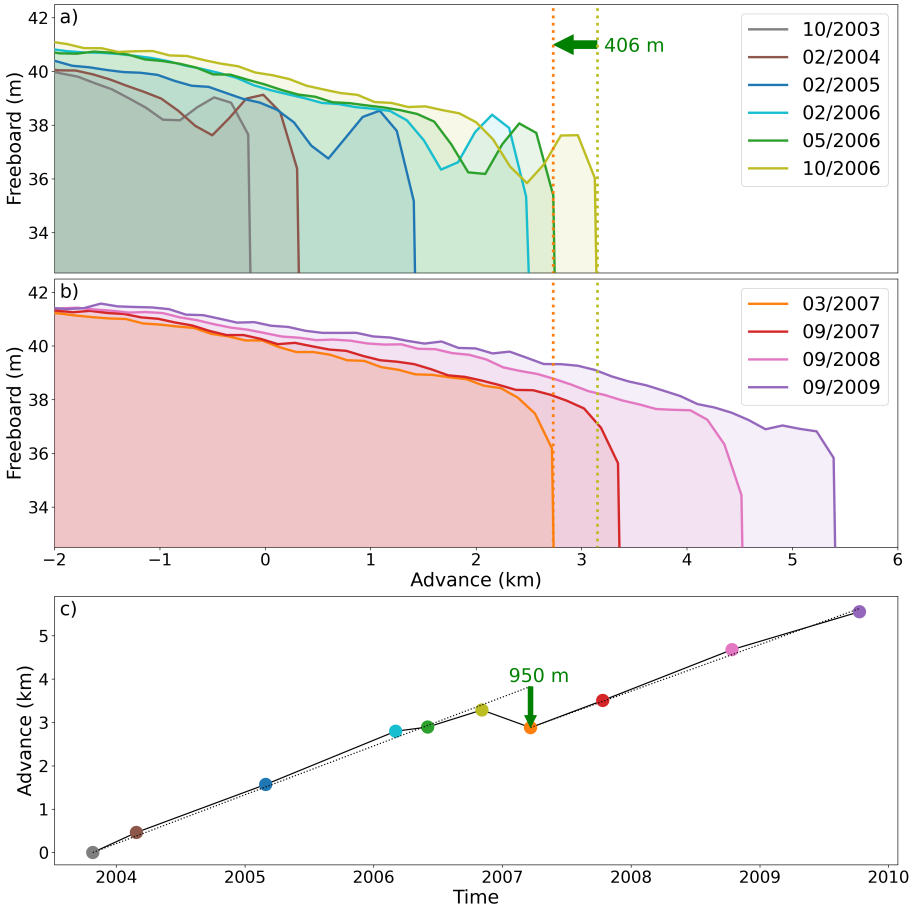

Figure 2. ICESat elevation data of the Ross Ice Shelf near-front region at 178.8°E. (a) Six profiles of freeboard elevation within $2-5$ km of the ice front, collected between October 2003 (gray) and October 2006 (yellow). The horizontal axis is set to zero at the front of the earliest profile. Clearly visible is the presence and growth of the rampart–moat shape. (b) Four elevation profiles collected between March 2007 and September 2009. The first two feature a standard berm shape, while the rampart–moat structure reemerges in the final two profiles. Between the October 2006 and February 2007 profiles, the front retreated by around 406 m (see vertical lines in panels a and b). This suggests a calving event of roughly 950 m, since the glacier also advanced 544 m in the intervening 4 months, assuming a nearly constant frontal advance speed of ≈ 1000 m/yr. This speed is estimated from a linear fit to the frontal advance plot in panel (c).

Ice-surface profiles from NASA's ICESat (2003–2009) and ICESat-2 (2018–present) laser altimetry missions provide two unique high-accuracy datasets that yield striking insights:

1. Figure 2 shows 10 repeat ICESat transects (track 0068 of the L2 Global Antarctic and Greenland Ice Sheet Altimetry data product, GLAH12, release 34; Zwally et al., 2014), with corrections for tides using CATS2008 (Padman et al., 2008; Howard et al., 2019), inverse barometer effects (Padman et al., 2003), and Gaussian-centroid bias (Borsa et al., 2014). The transects cross the Ross Ice Shelf front at 77.8 °S, 178.8 °E and were collected at roughly equal time intervals

https://doi.org/10.5194/egusphere-2024-571
Preprint. Discussion started: 26 March 2024

over 6 years. This time series appears to capture a full rampart–moat growth and calving cycle: starting in late 2003, the rampart–moat structure is clearly visible and becomes steeper over time, until a calving event occurs in late 2006, resetting the frontal profile to a classic berm shape and causing a retreat of the front of ≈ 1 km (Figure 2c). Following the calving event, the front advances again at the same speed as before the event, and a new rampart–moat start to form by 2009/2010. We note that to date the 2003–2010 ICESat record still spans a longer period than ICESat-2.

2. Using transects of ICESat-2 data collected between October 2018 and July 2020, Becker et al. (2021) showed that the rampart–moat shape is a characteristic feature found at approximately three quarters of the Ross Ice Shelf front. The presence of this smoothly undulating shape suggests that Ross Ice Shelf may have an underwater foot for much of its calving front. We manually classified the 3480 transects of the Becker et al. (2021) dataset according to the extent of near-frontal surface deflection: 2318 transects were excluded, either because they did not cross the front, featured large data gaps, or were not readily classifiable due to large crevasses that resulted in substantial elevation uncertainties. Among the 1162 remaining transects, 220 (∼20%) were found to feature downward-sloping berm profiles, and 942 (∼80%) transects exhibited rampart–moat shapes (Figure A1). Here, we will analyze the ICESat-2 transects that exhibit a rampart–moat shape and compare these to an elastic beam model.

For ICESat, the accuracy is 14 cm and the precision 2.1 cm (Shuman et al., 2006). For ICESat-2, accuracy is 3 cm and precision 9 cm (Brunt et al., 2019). Rampart–moat deformations are typically detected on $\sim 1-10$ m vertical scales, which suggests both satellites have sufficient accuracy and precision for the present purpose. ICESat-2 surpasses ICESat in two key aspects: footprint size (12 m vs. 70 m) and spatial resolution (40 m vs. 170 m). ICESat-2 therefore provides a much finer resolution of the rampart–moat profiles (which typically have a horizontal extent of a few hundred meters), whereas ICESat only captures a small number of points along a typical rampart-moat length.

3 Methods

3.1 Elastic beam representation

To gain physical insight into the deflection and calving process, we consider the highly idealized representation of the near-front ice shelf as a two-dimensional semi-infinite rectangular elastic plate of uniform thickness. Neglecting along-front variations, the model reduces to a 1-D elastic beam equation (Mansfield, 1964). A uniform buoyancy–weight force is applied along the beam, as well as a point force at the front, representing the effect of the foot. Implications of the various simplifying assumptions, such as a purely elastic rheology, uniform thickness, and lack of crevassing will be discussed in the following sections. The hydrostatic balance equation for such a floating beam of uniform thickness h can then be written as (e.g., Vella and Wettlaufer, 2008; Wagner et al., 2014):

$$B\frac{\mathrm{d}^4 w}{\mathrm{d}x^4} = \rho_w g d - \rho_i g h + Q\delta(x), \tag{1}$$

https://doi.org/10.5194/egusphere-2024-571
Preprint. Discussion started: 26 March 2024

where x is the distance perpendicular to the front, $w(x)$ the deflection of the beam centerline relative to the unperturbed isostatic equilibrium, d the draft (thickness of the submerged ice), ρ_i the density of ice, ρ_w the density of water and g the acceleration due to gravity. The flexural rigidity (or bending stiffness) of the beam is defined as $B \equiv \frac{1}{12} E h^3/(1-\nu^2)$, where E is the elastic modulus and ν the Poisson's ratio (fixed here at $\nu = 0.3$, a typical value for ice, see e.g., Vaughan, 1995). The first term on the right of (1) gives the upward acting buoyancy force and in isostatic equilibrium $d = h\rho_i/\rho_w$. The second term on the right represents the weight of the beam, and $Q\delta(x)$ describes the foot-induced point force of magnitude Q acting at the glacier front ($x = 0$), with $\delta(x)$ the Dirac delta function.

We apply clamped boundary conditions at $x \to \infty$ and free boundary conditions at $x = 0$. Further assuming an idealized full-depth rectangular foot of cross-sectional dimensions l_f and d, equation (1) can be solved for the foot-induced deflection, resulting in the well-known form of an exponentially decaying horizontal oscillation (e.g., Hetényi and Hetbenyi, 1946) :

$$w(x) = \sqrt{2}\mathcal{H} l_f \exp\left(\frac{-x}{\sqrt{2}l_w}\right) \cos\left(\frac{x}{\sqrt{2}l_w}\right), \tag{2}$$

where the characteristic buoyancy wavelength is defined as $l_w \equiv (B/\rho_w g)^{1/4}$, a measure of the energetic balance between beam bending and displacing water. Here, $\mathcal{H} \equiv (1-\rho_i/\rho_w)\, d/l_w$ is a scaled thickness related to the vertical dimension of excess buoyancy, such that the product $l_f\mathcal{H}$ determines the magnitude of the upward lift at the front.

For the observed ICESat(-2) surface profiles, we extract the horizontal distance between the ice front and the "moat location", x_{RM}, defined at the maximum depression at the center of the moat. To do so, each transect is projected onto the meridian of its mean longitude. Since most of the ice shelf front is close to zonal in its orientation, the meridional projection of a transect ensures that the profile runs approximately perpendicular to the ice front. We also measure the total vertical rampart–moat height difference $w_{RM} = w(0) - w(x_{RM})$, as indicated in Figure 1. These observed quantities can be compared to the beam model, since theoretical expressions for x_{RM} and w_{RM} are readily obtained from (2). We find

$$x_{RM} = 3\frac{\pi}{2\sqrt{2}} l_w, \tag{3}$$

$$w_{RM} = \left(\sqrt{2} + e^{-3\pi/4}\right) l_f \mathcal{H}. \tag{4}$$

Note that the location x_{RM} depends on the flexural rigidity alone (through l_w), and not on the size of the foot. The frontal uplift on the other hand scales with the foot volume $l_f d$ (per unit lateral width), and inversely with the buoyancy length l_w.

The stresses induced by bending will be largest at the bottom and top surfaces of the beam and reach a maximum at a distance $L = \pi/(2\sqrt{2}) l_w = x_{RM}/3$ from the ice front, which is the locus of maximum curvature. This maximum stress is then $\sigma_{\max} = Y \left|\frac{\mathrm{d}^2 w}{\mathrm{d}x^2}\right|_L$ (Mansfield, 1964), where $Y \equiv \frac{1}{2} E h/\left(1-\nu^2\right)$ is the stretching stiffness of the beam. Following Wagner et al. (2014), we assume that a calving event will be triggered at $x = L$ when the tensile stress at the base reaches the yield strength, σ_y, of the beam, i.e. when $\sigma_{\max} = \sigma_y$. Using this stress balance at the point of calving, and computing the curvature at $x = L$ from (2), we obtain following expression for the critical foot length to induce calving, $l_f^{\max}$ (Wagner et al., 2014):

$$l_f^{\max} = \frac{e^{\pi/4}}{6} \frac{\rho_w}{\rho_i g\left(\rho_w - \rho_i\right)} \frac{h}{l_w} \sigma_y. \tag{5}$$

https://doi.org/10.5194/egusphere-2024-571
Preprint. Discussion started: 26 March 2024

The calving event triggered when l_f reaches $l_f^{\max}$ will have the above-water length L and the underwater length $L + l_f^{\max}$. Finally, we note that, for simplicity, we do not include a downward bending moment that arises from the vertical differences between ice and water pressures at the ice front (Reeh, 1968). Mosbeux et al. (2020) showed that this downward bending will increase L by $15 - 50$ %, depending on the size of the foot, indicating that in this respect our calving size estimates represent lower bounds.

3.2 Wave-induced melting

In this framework, the frequency at which the foot-induced stresses trigger calving is determined by the rate of growth of the foot, i.e., $\mathrm{d}l_f/\mathrm{d}t$. This is closely related to the wave erosion of the ice cliff near the waterline, written as the melt rate, $r = \mathrm{d}m/\mathrm{d}t$, with m the melted distance perpendicular to the ice front. We assume that as waves melt a notch into the cliff the overhanging ice is continuously removed by frequent small-scale serac-type failure of the freeboard. If we further assume that the mean ambient melt of the draft is small compared to the wave-induced near-surface erosion (White et al., 1980), then the underwater foot grows at the same rate as the waves erode the cliff, i.e., $\mathrm{d}l_f/\mathrm{d}t = r$. The validity of the small ambient melt assumption will depend on the given environmental conditions. It is likely better satisfied in scenarios with strong temperature stratification and where there is sufficient open water near the ice front for substantial wave genesis. The assumption has been found to generally hold up well for icebergs drifting in open waters (e.g., Wagner and Eisenman, 2017), and we assume that the Ross Sea Polynya (discussed below) may allow for similarly high relative rates in wave-induced melt versus ambient melt. To our knowledge there is no existing parameterization of wave erosion at ice shelf fronts, so we draw on an empirical expression derived from laboratory experiments for floating ice blocks. Different versions of this have been used in the iceberg decay literature since the 1980ies (e.g., White et al., 1980; El-Tahan et al., 1987; Bigg et al., 1997). We adapt the form in Gladstone et al. (2001), which is an expression of the melt rate in terms of sea surface temperature, T, near-surface wind speed, $|\boldsymbol{u}|$, and sea ice concentration, c:

$$r = \tfrac{1}{2}\left(\alpha_1 + \alpha_2 T\right)\left(\beta_1\sqrt{|\boldsymbol{u}|} + \beta_2\,|\boldsymbol{u}|\right)\left(1 + \cos\left[\pi c^3\right]\right). \tag{6}$$

We use the empirical parameters from Martin and Adcroft (2010), as written in England et al. (2020): $\alpha_1 = 0.67$, $\alpha_2 = 0.33\ ^\circ\mathrm{C}^{-1}$, $\beta_1 = 8.7 \times 10^{-6}\ \mathrm{m}^{1/2}\,\mathrm{s}^{-1/2}$, and $\beta_2 = 5.8 \times 10^{-7}$. The wind speed term is invoked to represent wave energy, using a relation between the Beaufort Scale and the sea state (Bigg et al., 1997). Note that (6) is a local parameterization of the wave-induced melt rate, not taking into account non-local processes such as swell generated in the open ocean. Furthermore, we emphasize that (6) has not been validated comprehensively against real-world conditions and therefore contains large uncertainties. We calculate a wave-induced melt rate climatology at Ross Ice Shelf from observed monthly environmental fields T, $|\boldsymbol{u}|$, and c, provided by the data sets discussed below in Section 3.3. As there is substantial uncertainty and variability in the environmental fields at the ice–ocean boundary, we take the mean over an ocean strip along Ross Ice Shelf that extends 60 km seaward from the shelf front (see Figure 3). The resulting melt rate estimates are not very sensitive to the exact choice of strip width (not shown).

https://doi.org/10.5194/egusphere-2024-571
Preprint. Discussion started: 26 March 2024

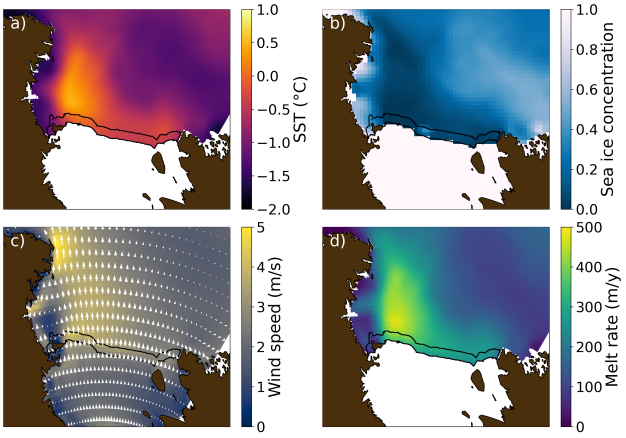

Figure 3. Environmental properties in the Ross Sea and corresponding local melt rate estimate derived from the listed observations and reanalysis. Shown are January fields averaged over 2003–2022 for (a) SST (GHRSST from NASA/JPL, 2015), (b) SIC (NSIDC Climate Data Record from Meier et al., 2021), (c) wind velocities (ERA-5 from Hersbach et al., 2023), and (d) melt rate computed from the other fields using equation (6). The 60 km near-frontal strip over which the environmental variables are averaged is indicated in all panels (black contour).

3.3 Ross Sea environmental data

The melt parameterization (6) incorporates sea surface temperature (SST), near-surface wind speeds, and sea ice concentration (SIC). Here, we use the Group for High Resolution Sea Surface Temperature (GHRSST) product at 0.01° resolution (NASA/JPL, 2015) for SST, the ERA-5 monthly reanalysis product (Hersbach et al., 2023) for 10 m surface wind speed (with native horizontal resolution 0.25°), and the National Snow and Ice Data Center Climate Data Record v.4 satellite SIC monthly dataset at 25 km resolution (Meier et al., 2021). All datasets are monthly averaged over the years 2003–2022 to compute a climatological mean estimate of melt rates, and they were regridded to the regular GHRSST 0.01° grid without interpolation.

3.4 Calving frequency and volume

Some Antarctic ice shelves are marked by regularly spaced crevasses (see, e.g., front of the Thwaites Glacier, Figure A2). In these cases, calving rates are understood to be determined by crevasse spacing, ice flow speed, and associated ice shelf thinning, which will eventually lead to tensile stresses that are large enough to open up the crevasses such that calving occurs (e.g., Buck, 2023). For steady ice velocities this would suggest regular calving events of a given characteristic size (set by the crevasse spacing). For a given calving frequency f and characteristic calving length L in the direction of flow, the rate of ice loss from calving, C (retaining the assumptions of uniform thickness and no along-front variability) is then simply $C = f\,L$. Here, C is measured as distance per unit time of ice lost in the direction perpendicular to the ice front.

For Ross Ice Shelf, large crevasses are much rarer and unevenly spaced (Figure A2). Although this leads to infrequent calving of giant icebergs, at least some of the frontal balance is likely maintained by smaller-scale calving events (sometimes

https://doi.org/10.5194/egusphere-2024-571
Preprint. Discussion started: 26 March 2024

185 referred to as edge-wasting; Scambos et al., 2005), which we suggest include footloose-type calving. For footloose calving, we combine the beam model with the estimated melt rates from (6), assuming that calving occurs each time when the melt distance m is equal to a foot of size $l_f = l_f^{\max}$. This gives a calving frequency $f = r/l_f^{\max}$. The time-averaged ice loss rate due to footloose-type calving is then written as

$$C = \frac{r}{l_f^{\max}} L. \tag{7}$$

190 This allows an assessment of how the footloose-induced calving rate depends on environmental factors and ice thickness, as well as on the material properties B and σ_y. It further enables us to put this calving process in relation with the total frontal mass balance of the ice shelf.

4 Results and Discussion

4.1 Beam theory fit to observations

195 We first assess whether the idealized floating beam experiencing a point force at its front describes an ice shelf that is consistent with the satellite observations. We do so by comparing the beam solution (2) to the ICESat-2 transects that were identified as featuring rampart–moat profiles.

In order to directly compare profiles with different rampart–moat heights and horizontal extents, we normalize the observed transects. This is done by scaling the horizontal dimension by an observational estimate of l_w^{obs}, which is computed from the
200 observed distance x_{RM} using (3). The vertical dimension can similarly be scaled by $w(0)$, which is obtained from the observed w_{RM} using (2) and (4). In Figure 4 we show the resulting dimensionless ICESat-2 transects, together with the dimensionless solution $W(X)$ of equation (2). Here, $W = w/w\,(0)$ and $X = x/l_w^{\text{obs}}$, such that the frontal elevation $W(0) = 1$, and the moat location $X_{RM} = 3\pi/(2\sqrt{2})$. Note that we also shift the observed transects vertically, so that the frontal height is equal 1.

Figure 4a shows general agreement between the transects and the beam solution. We excluded all transects that feature
205 downward-sloping berm profiles as well as small upward deflections ($w_{RM} < 2$ m), since in these cases other small-scale features in the ice surface profile lead to rather noisy profiles once they are scaled by the small frontal uplift. We further excluded transects featuring a mix of rampart–moat and berm characteristics. Figure 4b and 4c show that the moat position ranges between $x_{RM} = 150 - 750$ m (with most values $250 - 500$ m) and the frontal uplift is $w_{RM} = 2 - 15$ m (with a peak at about 6 m).

210 It is apparent from Figure 4 that the ice shelf thickens with distance from the front, indicated by the increasing surface elevations with increasing x. The theoretical solution (for a fixed thickness beam with $w \to 0$ for $x \to \infty$) and the observed surface profiles therefore diverge as x becomes large, leading to a vertical mismatch of up to 6 m at a distance of 1500 m from the ice front. Vertical scales in Figure 4 are greatly amplified, and under the assumption of isostatic balance the results above suggest that the ice shelf thins by less than 40 m/km = 0.04 near the ice front (but away from the rampart–moat). The
215 assumption of uniform thickness should thus be largely satisfied near the ice front.

https://doi.org/10.5194/egusphere-2024-571
Preprint. Discussion started: 26 March 2024

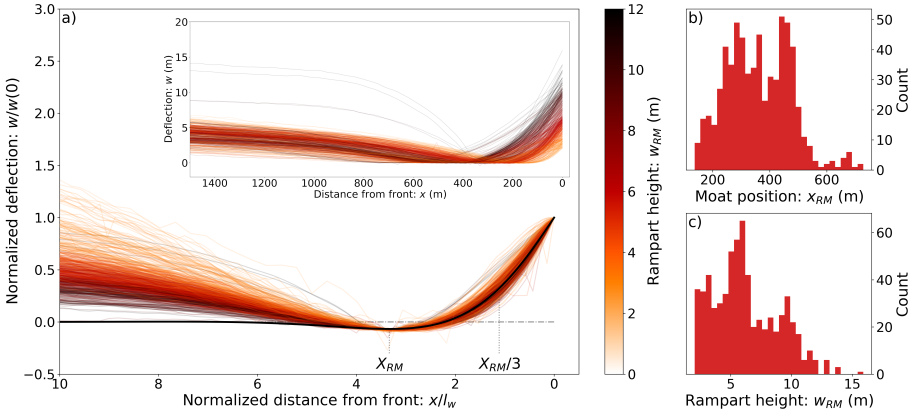

Figure 4. Ross Ice Shelf front elevation profiles. (a) Normalized ICESat-2 transects (thin colored lines), with dimensionless 1D elastic beam solution in black. Shown are the subset of 654 transects which feature $w_{RM} > 2$ m. The divergence in lighter curves with distance from the ice edge is a result of these transects being vertically scaled by smaller values of w_{RM}. Also indicated by dotted vertical lines are the location of maximum depression, X_{RM}, and the location of maximum stress, $X_{RM}/3$. Inset: same as main figure, but without normalization. Here, the transects were vertically shifted such that $w(x_{RM}) = 0$. (b) Histogram of moat positions, corresponding to transects in panel a. (c) Histogram of rampart heights, corresponding to transects in panel a.

The results in Figure 4 are subject to the assumption that the beam relations (3) and (4) hold for each observed transect. The buoyancy length l_w^{obs} is thus treated as a free parameter that can be independently computed from x_{RM} for all individual transects. Beam theory states, however, that the buoyancy length is determined by the elastic modulus, E, and ice thickness, h, such that $l_w \sim E^{1/4}h^{3/4}$ (see above). Since E is typically considered a known material parameter and since h can be estimated from the observed freeboard, it may be expected that l_w is readily constrained. To test this, we consider an elastic modulus value used in the literature for ice shelves, $E = 1$ GPa (e.g., Vaughan, 1995), which is about an order of magnitude lower than laboratory values for pure ice. We note that values of $E \sim 1$ GPa are typically inferred from tidal flexure near the grounding line, and the effective modulus near the calving front may be different. We estimate h at the front from the observed freeboard for each transect using a depth-averaged ice density of 850 kg/m^3, taking into account the less dense firn layer (Drews et al., 2016). Computing l_w this way, and comparing it to l_w^{obs} obtained from (3), we find a persistent mismatch, with the theoretical l_w larger than l_w^{obs} by a factor of 5 to 8 (Figure A3).

The discrepancy between the anticipated theoretical buoyancy length and the observed length scales of deformation has been encountered in previous studies that apply an elastic framework to frontal ice shelf bending (Scambos et al., 2005; Wagner et al., 2016; Mosbeux et al., 2020). We suggest that this is due to two main factors: (1) the ice undergoes viscous creep on the timescale of rampart–moat development (i.e., years; Figure 2) and plastic failure, impacting the deformation on the time scales relevant here, as discussed further below; (2) the ice shelf is not a uniform and homogeneous beam, but rather features crevasses, smaller-scale damage, a firn layer, temperature gradients, and more. These factors predominantly act to reduce the flexural rigidity, B, and thereby the buoyancy length of the ice shelf, relative to that of a perfect beam of ice.

https://doi.org/10.5194/egusphere-2024-571
Preprint. Discussion started: 26 March 2024

It has been argued that this weakening of B is primarily due to a lowered elastic modulus in the ice shelf. Mosbeux et al. (2020), for example, discuss this issue and offer three main reasons for a depressed elastic modulus: softening due to temperatures near melting and associated strain-rate effects; infiltration of sea water at the firn–ice interface; and the presence of ice damages and crevasses. This has been used to suggest an "effective" elastic modulus (Cuffey and Paterson, 2010) that may be substantially lower than standard values. Mosbeux et al. (2020) argue for an effective elastic modulus E^* as low as 2 MPa for the Ross Ice Shelf front, which leads to a reduction in l_w by roughly 80%, compared to $E = 1$ GPa. We note that Jenkins et al. (2006) argue that a reduced buoyancy length may also be due to a higher effective Poisson's ratio in the ice shelf.

Here, we consider the perspective suggested by Scambos et al. (2005) that crevasses and damages may result in a lower effective ice thickness, h^*, rather than a lower value for E. We thus write $B^* = Eh^{*3}/12(1-\nu^2)$. As a first approximation, we assume that the effective ice thickness is reduced throughout the shelf by a constant fraction, a, relative to the the full thickness, such that $h^* = ah$ and $l_w^* = a^{3/4} l_w$. We note that this is mathematically equivalent to taking $E^* = a^3 E$. For example, lowering E from 1 GPa to 1MPa sets $a = 0.1$ and is equivalent to taking $h^* = 0.1h$. This gives $l_w^* = 0.18 l_w$ and results in close correspondence between l_w^* and l_w^{obs} (Figure A3).

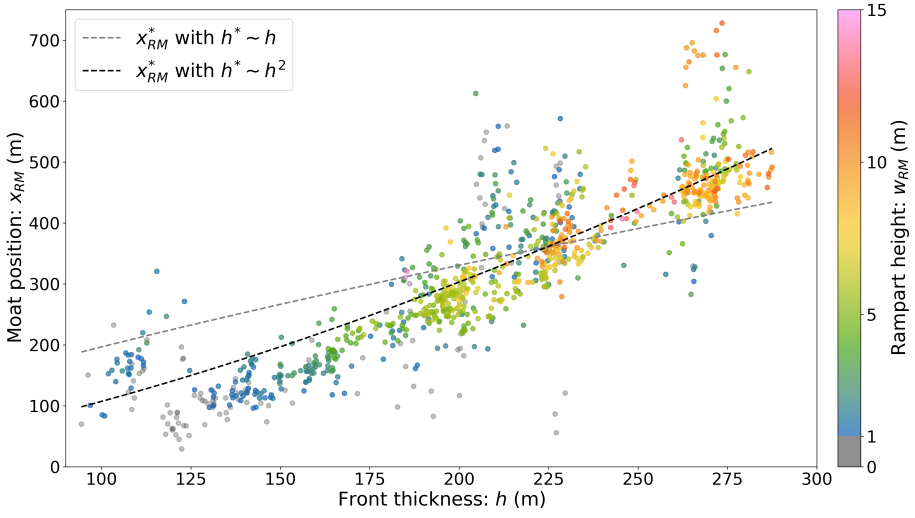

Figure 5. Moat position x_{RM} predicted by the elastic beam theory (dashed lines) and measured from ICESat-2 transects (circles) as a function of the front thickness, h. Shown are the theoretical relations $x^*_{RM}(h)$ for $h^* \sim h$ (gray) and $h^* \sim h^2$ (black). Circle colors indicate the values of the observed rampart–moat height w_{RM}.

We can now compute a theoretical estimate for $x^*_{RM}(h) = 3\pi/(2\sqrt{2}) l^*_w(h)$ and compare this to the observed relation between x_{RM} and h (Figure 5). The theoretical and observed values show good agreement in overall values, but the theoretical range $x^*_{RM} \approx 200 - 400$ m is smaller than the observed $x_{RM} = 100 - 700$ m. Furthermore, $x^*_{RM} \sim h^{3/4}$, whereas a best fit to the observations reveals an approximate scaling of $x_{RM} \sim h^{3/2}$.

This discrepancy can be resolved by relaxing the assumption that the effective ice thickness is a constant fraction of the actual thickness. If we instead use a quadratic scaling, $h^* = ah^2$, which implies that the relative effective thinning is more pronounced

https://doi.org/10.5194/egusphere-2024-571
Preprint. Discussion started: 26 March 2024

for thinner ice than for thicker ice, we obtain a close fit between the observed and modeled x_{RM} (black dashed curve in Figure 5). In other words, by allowing for one additional free parameter (the exponent of h), we achieve good agreement between the observed and theoretical horizontal lengths of the rampart–moat profiles across the Ross Ice Shelf front. Physically, this may be interpreted as having an effective thickness, h^*, that gets closer to the actual thickness, h, as h increases (for the observed range of h). This could be the case if, for example, crevasses have a constant penetration depth: then for thicker ice the relative degree of crevassing is lower. By caveat, however, we note that this improved fit in the horizontal dimension comes at a cost of a reduced fit in the vertical dimension (see below).

We see from Figure 5 that w_{RM} increases with h. The observed relation scales roughly as $w_{RM} \sim h^{1.7}$ (Figure A4), while elastic beam theory predicts $w_{RM} \sim h^{1/4}$ when $h^* \simeq h$ (equation 4), and $w_{RM} \sim h^{-1/2}$ when $h^* \sim h^2$. There are several possible explanations for this discrepancy: (i) the foot-induced hydrostatic imbalance may skew the freeboard-to-height conversion at the front; (ii) there may be increased basal melt at thinner parts of the ice shelf which could also suppress foot growth (and hence upward deflection) for those regions; (iii) internal bending moments due to temperature gradients in the ice increase with ice thickness. Notably, it has been shown that for deformations due to internal moments the uplift scales with $h^{3/2}$, in good agreement with the observed scaling (Buck, 2024). However, the magnitudes of uplift observed in ICESat-2 are only achieved by the internal bending process for activation energies that are higher than standard values. This suggests that the foot-induced and internal bending stresses may act together to cause the observed uplift.

4.2 Estimation of characteristic calving length

Figure 5 reveals that for the observed transects, $x_{RM} = 90 - 710$ m, which according to the theory suggests calving sizes of $L = x_{RM}/3 = 30 - 210$ m. As a ballpark average value for Ross Ice Shelf to be used in the calving rate equation (7), we consider the approximate mean frontal thickness $h = 200$ m along Ross Ice Shelf, which gives $L \approx 110$ m (Figure 5). We emphasize that this characteristic calving size L is independent of the yield strength σ_y, since the value σ_y does not impact the location of maximum stress but rather determines the upper bound foot length $l_f^{\max}$ before calving.

The observed frontal uplift w_{RM}, in combination with the fitted l_w^* can be used to compute theoretical foot lengths, which range between $l_f = 0 - 32$ for both scalings of h^* (Figure 6). This is broadly in agreement with underwater feet observed in other settings (e.g., Wagner et al., 2014), and the upper bound of $l_f^{\max} \approx 30$ m appears consistent with the image of the calved iceberg in Figure 1c.

Using the estimated $l_w^* = 91$ m (where $h^* \sim h$) for an ice thickness $h = 200$ in equation (5) we find $l_f^{\max} = 88$ m for $\sigma_y = 100$ kPa (a value given for example in Bassis and Jacobs, 2013). If we adopt a lower value of $\sigma_y = 50$ kPa as an effective yield strength (indicative of substantial crevassing), the critical foot size is $l_f^{\max} = 44$ m, which would be in good correspondence to the maximum foot length as estimated from the ICESat-2 transects in Figure 6. We will use this value of $l_f^{\max}$ for the estimation of a footloose calving frequency, as discussed next. In reality the actual size of calving will likely be determined by pre-existing basal crevasses near the ice front, which the bending stresses will open up, eventually leading to calving. Requiring relatively low values of σ_y to trigger calving in this framework suggests that the bending stresses alone may not be sufficient to initiate crevassing.

https://doi.org/10.5194/egusphere-2024-571
Preprint. Discussion started: 26 March 2024

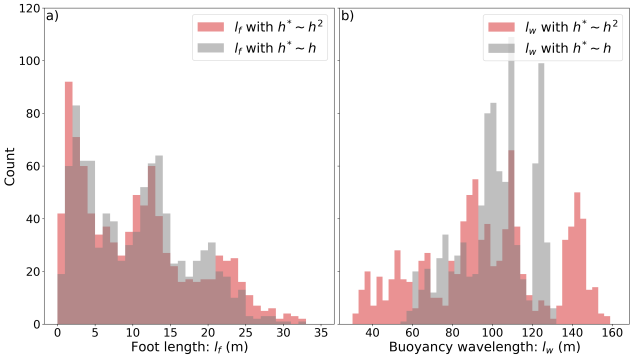

Figure 6. Histograms of estimated (a) foot length l_f, and (b) buoyancy length l_w^*, for $h^* = a_1 h$, with $a_1 = 0.1$ (gray), and $h^* = a_2 h^2$, with $a_2 = 5 \times 10^{-4}$/m (red).

4.3 Melt rate estimation and calving frequency

The climatological January fields of SST and SIC in Figures 3a and b show the presence of the large Ross Sea Polynya, extending over the entire length of the Ross Ice Shelf front. This is consistent with the katabatic winds of Figure 3c, blowing down the ice shelf roughly in parallel with the ice flow direction and pushing the sea ice northward. The polynya allows for greatly enhanced solar heat uptake by the near-shelf ocean. This has been shown to have profound impacts on basal melt rates of the ice shelf (Stewart et al., 2019), but the potential impact on frontal melt has not been studied in detail. The polynya is likely a key factor for wave-induced melting since it allows for both surface heating and for notable wave energy near the front. As a result, equation (6) estimates January melt rates close to zero to the west of Ross Island where there is substantial sea ice cover and above 200 m/yr for the rest of the ice shelf where SIC is near zero at this time of year (Figures 3d and 7).

Figure 7 shows the monthly climatological melt rate along the ice shelf front, averaged over the years 2004–2022 and using the 60 km near-front swath indicated in Figure 3d. As expected, melt rates are highest in January (with the along-front mean topping out at ≈300 m/yr) and consistently low in winter, which is due to low T and due to melt rates reducing rapidly for $c > 0.5$ in the $\cos(\pi c^3)$ term. The along-front mean winter melt is around 20 m/yr from April through October. This may still be biased high, given the substantial uncertainties in both the environmental data along the ice shelf front and in the parameterization itself. Averaging over the yearly cycle, we find an annual mean melt rate $r = 80$ m/yr. Comparing this to $l_f^{\max} = 44$ m from the previous section (for $h = 200$ m and $\sigma_y = 50$ kPa), this suggests a calving frequency of $f \approx 2$/yr. This number is only weakly sensitive to changes in h and E due to the 1/4 power scaling in (5), but scales linearly with σ_y. For example, a yield strength $\sigma_y = 100$ kPa will double $l_f^{\max}$ and thereby reduce the calving frequency to ≈ 1 per year.

4.4 Calving rate

Using the characteristic calving size $L = 110$ m for $h = 200$ m and the corresponding frequency $f = 2$/yr, we estimate that the annual-mean ice loss due to footloose-type calving at Ross Ice Shelf is of the order $C = fL \sim 220$ m/yr. Together with

https://doi.org/10.5194/egusphere-2024-571
Preprint. Discussion started: 26 March 2024

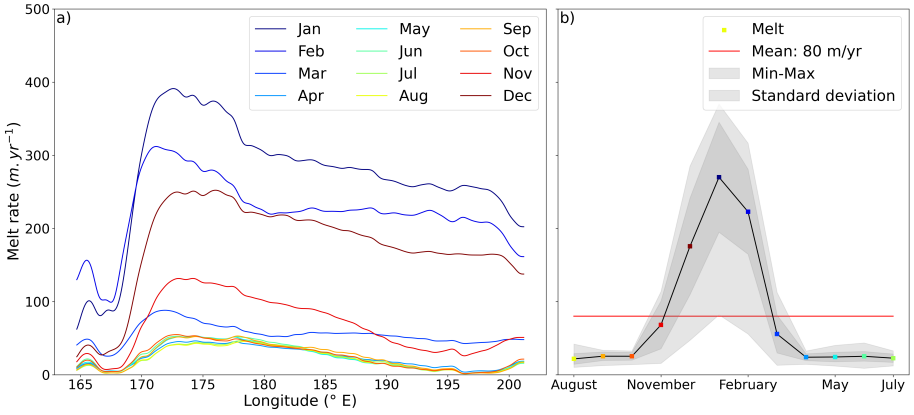

Figure 7. Wave induced melting along the Ross Ice Shelf front computed from the melt rates shown in Figure 3d. a) Climatological melt (averaged over 2003–2022) as a function of longitude, computed using the 60 km-wide near-front ocean swath of Figure 3. b) Zonally averaged climatology with the mean annual melt rate shown by the red line.

the frontal melt rate of 80 m/yr, this would suggest total wave-induced ice loss of ~ 300 m/yr. There is substantial spatial and temporal variability in this system, and these numbers are merely intended as back-of-envelope estimates.

The time series of Figure 2 exhibits some differences to these theoretical results: (i) ICESat profiles only feature one clear calving event over the 6 year period from 2004–2010, and the observed rampart–moat profile in this case grew over multiple years, rather than the $6-12$ month time scale we estimated above. (ii) The observed calving event in late 2006 led to a frontal retreat of about 940 m, larger than the estimated characteristic calving lengths of $L \sim 100$ m. (iii) The speed of frontal advance in Figure 2 is close to 1000 ± 25 m/yr which is similar to observed ice flow speeds at this location from satellite and in situ data (1030 ± 50 m/yr, Klein et al., 2020; Mosbeux et al., 2023). This suggests that the frontal melt rate of 80 m/yr is biased high since such fast melt would be expected to result in a divergence of the frontal ice flow speed and the frontal advance. Assuming that the time series of Figure 2 captures most of a full cycle of calving and rampart–growth, the calving rate inferred from the ICESat time series is $C = 1/(6\text{yr}) \times 940$ m $= 160$ m/yr. This is rather close to our theoretical estimate, but it appears that this agreement is at least to some degree coincidental.

A major reason for the discrepancies between the observations and theoretical estimates is likely the assumption of purely elastic deformation. Viscous flow almost certainly plays a role on the relatively long timescales over which the foot grows and the rampart–moat profile develops. Some of the l_w fitting needed above is also likely a result of having to compensate for the missing viscous effects.

The importance of viscous versus elastic deformation can be assessed by considering the Deborah number (Huilgol, 1975), defined as $De \equiv \tau_B/\tau$, where τ_B is the bending timescale and τ is the timescale of the process in question. Sayag and Worster (2013) estimated that for viscous flow, the relaxation timescale under bending for ice shelves is $\tau_B = 0.15-21$ yr, with $De \gg 1$ given a predominantly elastic process (which is easily satisfied, for example, for the case of tidal flexure with a time scale of ~ 12 h). Our results give $\tau \sim 0.5$ yr for the theoretical foot growth rate, while the ICESat timeseries suggests $\tau \sim 5$ yr. This

https://doi.org/10.5194/egusphere-2024-571
Preprint. Discussion started: 26 March 2024

entails rough ranges of $De = 0.3 - 10$ for the theory and $De = 0.03 - 4$ for the observations, indicating that viscous relaxation may play an important, if not dominant, role under certain conditions. This picture is further complicated by the foot growth process itself likely being marked by a series of small-scale calving events of the freeboard, with corresponding bending responses that have both fast elastic and slower viscous time scales.

Mosbeux et al. (2020) provide a detailed study of how viscous versus elastic processes influence the footloose calving mechanism. The authors find that accounting for viscous relaxation will lead to critical stresses being reached more gradually, relative to the elastic framework, and critical foot lengths for a given yield stress are $20 - 30\%$ larger in the viscous framework than the elastic framework. This may explain some of the timescale discrepancies between theory and observations. Notably, Mosbeux et al. (2020) argue that viscous effects lead to the maximum location of maximum stress moving closer to the ice front as the foot grows, which in turn would cause smaller-size calving events than the elastic case. In this respect, accounting for viscous relaxation would act to reconcile the theoretical estimates with the observed x_{RM} from ICESat-2 data, but not with the large-scale event from the ICESat time series. Other processes, such as the internal bending moments due to thermal gradients mentioned above may constitute important additional controls on the calving cycle.

5 Conclusions

The environmental conditions at the front of Ross Ice Shelf are conducive to the development of buoyant underwater feet, and anecdotal evidence such as the image of a calved iceberg near Ross Island (Figure 1c) and the ICESat timeseries in Figure 2 suggest that footloose-type calving may be an important process in controlling the Ross Ice Shelf frontal mass balance. We have shown that the widespread rampart–moat profiles found for ICESat-2 transects are broadly consistent with an elastic beam model. However, crevassing and viscous effects likely play non-negligible roles in determining the observed deformations and resultant calving pattern. Our results suggest a characteristic iceberg calving size of $L \sim 100$ m associated with footloose-type calving. We estimate that averaged over time, this process contributes a loss of $\sim 200 - 300$ m/yr along the front of Ross Ice Shelf. Compared to a frontal advance of ~ 1000 m/yr for much of the central ice shelf, this suggests that footloose calving may contribute around a quarter of the total mass loss. We further estimate that frontal melt due to wave erosion contributes up to 80 m/yr. Much of the remainder of the frontal mass balance is likely due to sporadic rifting and calving of large tabular icebergs. Under continued future warming and associated increases in sea ice free periods, near-frontal wave energy, and ocean heat uptake, calving rates due to bending stresses at the ice shelf front may be expected to increase, with implications for the frontal mass balance and iceberg production. Further investigations are therefore warranted to reduce the substantial uncertainties persisting in the estimation of the frontal mass balance for Antarctica's ice shelves.

Code and data availability. Code to download data, perform data analysis, plot figures is available at https://github.com/nicsar2/FootlooseCalvingMechanism.git . Sea ice concentration data are available at https://nsidc.org/data/g02202/versions/4 . Wind speed data are available at https://doi.org/10.24381/cds.6860a573 .

https://doi.org/10.5194/egusphere-2024-571
Preprint. Discussion started: 26 March 2024

Sea surface temperature data are available at https://podaac.jpl.nasa.gov/dataset/MUR-JPL-L4-GLOB-v4.1 .

Becker et al. (2021) code repository to pre-process ICESat-2 transects is available at https://zenodo.org/records/4697517 .

ICESat-2 version 3 ATL06 data are available at https://nsidc.org/data/atl06/versions/6 .

GLAH12 release 34 data are available at https://nsidc.org/data/glah12/versions/34 .

https://doi.org/10.5194/egusphere-2024-571
Preprint. Discussion started: 26 March 2024

Appendix A

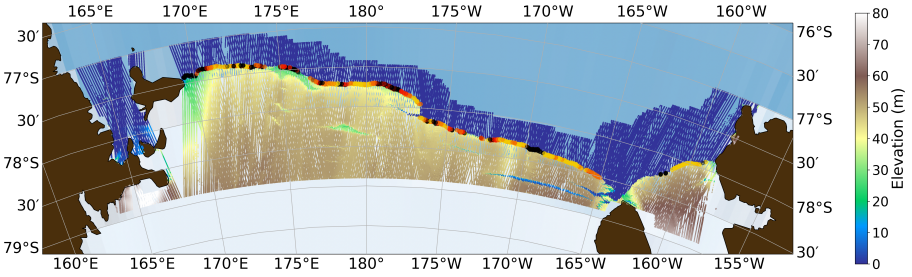

Figure A1. Elevation map of the Ross Ice Shelf front from ICESat-2 transects. Rampart–moat profiles detected are marked with a dot, color-coded according to the height: no rampart–moat or below 1 m (black), $1-2$ m (yellow), $2-5$ m (orange), and above 5 m (red). Land is shown in brown.

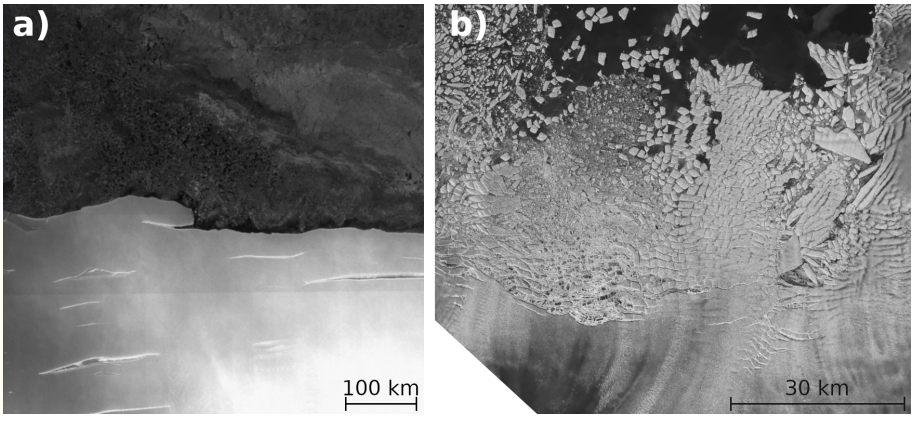

Figure A2. a) Part of the central Ross Ice Shelf front, photo from Copernicus Sentinel data 2023. Retrieved from ASF DAAC on 11/30/2023, processed by European Space Agency (ESA). **b)** Images of Thwaites Glacier Ice Tongue from April 2018 extracted from video by the Copernicus Sentinel-1 mission between 14 June 2017 and 7 July 2019, processed by ESA.

https://doi.org/10.5194/egusphere-2024-571
Preprint. Discussion started: 26 March 2024

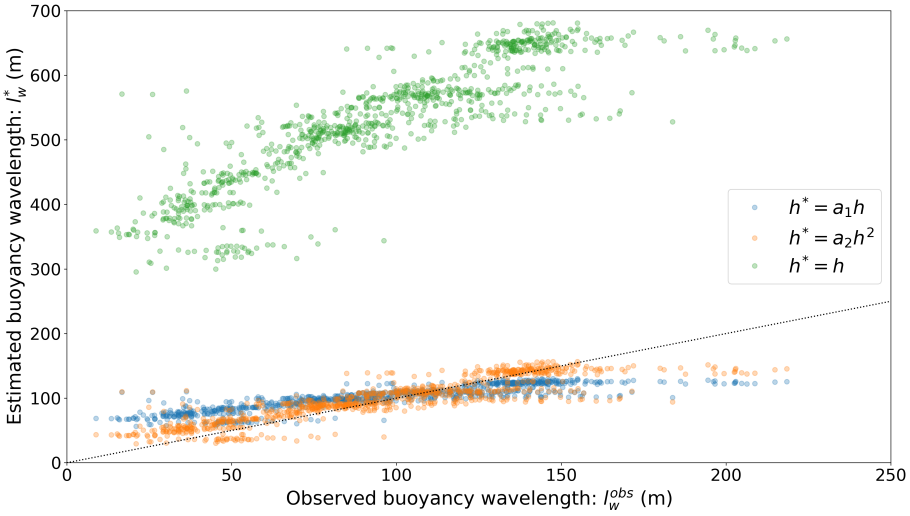

Figure A3. Comparison between the buoyancy wavelength l_w^{obs}, calculated from the beam theory using the observed rampart–moat position x_{RM}, and three approaches to estimate l_w^* from the bending stiffness B^* with different effective thicknesses h^* (see legend). Here $a_1 = 0.1$ and $a_2 = 5 \times 10^{-4}$/m.

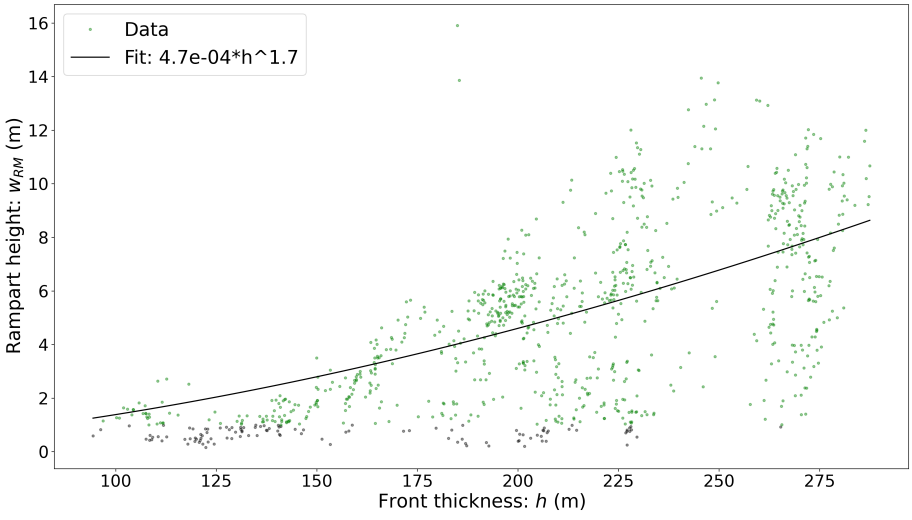

Figure A4. Rampart height as a function of estimated frontal thickness. Points are extracted from observed transects, classified by $w_{RM} > 1$ m (green) and $w_{RM} < 1$ m (gray). The black line represents a best fit (see legend).

https://doi.org/10.5194/egusphere-2024-571
Preprint. Discussion started: 26 March 2024

Author contributions. TJWW conceived the study idea. TJWW, NS, NP, and LKZ devised the methodology. NS carried out the analysis. MRS found and processed the ICESat time series of Figure 2. NS wrote the first draft with guidance from TJWW. All authors contributed to the interpretation of results and the writing of the manuscript.

Competing interests. The authors declare no competing interests.

370 *Acknowledgements.* The authors thank Maya Becker, Emily Glazer, and Roger Buck for helpful discussions.

https://doi.org/10.5194/egusphere-2024-571
Preprint. Discussion started: 26 March 2024

References

Abib, N., Sutherland, D. A., Amundson, J. M., Duncan, D., Eidam, E. F., Jackson, R. H., Kienholz, C., Morlighem, M., Motyka, R. J., Nash, J. D., et al.: Persistent overcut regions dominate the terminus morphology of a rapidly melting tidewater glacier, Annals of Glaciology, 38, 1–12, 2023.

Alley, R., Cuffey, K., Bassis, J., Alley, K., Wang, S., Parizek, B., Anandakrishnan, S., Christianson, K., and DeConto, R.: Iceberg Calving: Regimes and Transitions, Annual Review of Earth and Planetary Sciences, 51, 189–215, 2023.

Bassis, J. N. and Jacobs, S.: Diverse calving patterns linked to glacier geometry, Nature Geoscience, 6, 833–836, 2013.

Becker, M. K., Howard, S. L., Fricker, H. A., Padman, L., Mosbeux, C., and Siegfried, M. R.: Buoyancy-driven flexure at the front of Ross Ice Shelf, Antarctica, observed with ICESat-2 laser altimetry, Geophysical Research Letters, 48, e2020GL091 207, 2021.

Benn, D. I., Cowton, T., Todd, J., and Luckman, A.: Glacier calving in Greenland, Current Climate Change Reports, 3, 282–290, 2017.

Bigg, G. R., Wadley, M. R., Stevens, D. P., and Johnson, J. A.: Modelling the dynamics and thermodynamics of icebergs, Cold Regions Science and Technology, 26, 113–135, 1997.

Borsa, A., Moholdt, G., Fricker, H., and Brunt, K. M.: A range correction for ICESat and its potential impact on ice-sheet mass balance studies, The Cryosphere, 8, 345–357, 2014.

Brunt, K., Neumann, T., and Smith, B.: Assessment of ICESat-2 ice sheet surface heights, based on comparisons over the interior of the Antarctic ice sheet, Geophysical Research Letters, 46, 13 072–13 078, 2019.

Buck, W. R.: The role of fresh water in driving ice shelf crevassing, rifting and calving, Earth and Planetary Science Letters, 624, 118 444, 2023.

Buck, W. R.: The effect of ice rheology on shelf edge bending, EGUsphere, 2024, 1–17, https://doi.org/10.5194/egusphere-2024-557, 2024.

Buck, W. R. and Lai, C.-Y.: Flexural control of basal crevasse opening under ice shelves, Geophysical Research Letters, 48, e2021GL093 110, 2021.

Cuffey, K. M. and Paterson, W. S. B.: The physics of glaciers, Academic Press, 2010.

Drews, R., Brown, J., Matsuoka, K., Witrant, E., Philippe, M., Hubbard, B., and Pattyn, F.: Constraining variable density of ice shelves using wide-angle radar measurements, The Cryosphere, 10, 811–823, 2016.

El-Tahan, M., Venkatesh, S., and El-Tahan, H.: Validation and quantitative assessment of the deterioration mechanisms of Arctic icebergs, Journal of Offshore Mechanics and Arctic Engineering, https://doi.org/10.1115/1.3256983, 1987.

England, M. R., Wagner, T. J. W., and Eisenman, I.: Modeling the breakup of tabular icebergs, Science advances, 6, eabd1273, 2020.

Fox-Kemper, B., Hewitt, H. T., Xiao, C., Aðalgeirsdóttir, G., Drijfhout, S. S., Edwards, T. L., Golledge, N. R., Hemer, M., Kopp, R. E., Krinner, G., et al.: Ocean, cryosphere, and sea level change, in: Climate Change 2021: The Physical Science Basis. Contribution of Working Group I to the Sixth Assessment Report of the Intergovernmental Panel on Climate Change, pp. 1211–1361, Cambridge University Press, 2021.

Gladstone, R. M., Bigg, G. R., and Nicholls, K. W.: Iceberg trajectory modeling and meltwater injection in the Southern Ocean, Journal of Geophysical Research: Oceans, 106, 19 903–19 915, https://doi.org/https://doi.org/10.1029/2000JC000347, 2001.

Golledge, N. R., Keller, E. D., Gomez, N., Naughten, K. A., Bernales, J., Trusel, L. D., and Edwards, T. L.: Global environmental consequences of twenty-first-century ice-sheet melt, Nature, 566, 65–72, https://doi.org/10.1038/s41586-019-0889-9, 2019.

Greene, C. A., Gardner, A. S., Schlegel, N.-J., and Fraser, A. D.: Antarctic calving loss rivals ice-shelf thinning, Nature, 609, 948–953, 2022.

https://doi.org/10.5194/egusphere-2024-571
Preprint. Discussion started: 26 March 2024

Hersbach, H., Bell, B., Berrisford, P., Biavati, G., Horányi, A., Muñoz Sabater, J., Nicolas, J., Peubey, C., Radu, R., Rozum, I., Schepers, D., Simmons, A., Soci, C., Dee, D., and Thépaut, J.-N.: ERA5 monthly averaged data on pressure levels from 1940 to present. Copernicus Climate Change Service (C3S) Climate Data Store (CDS), https://doi.org/10.24381/cds.6860a573, 2023.

Heténi, M. and Hetbenyi, M. I.: Beams on elastic foundation: theory with applications in the fields of civil and mechanical engineering, vol. 16, University of Michigan Press, Ann Arbor, MI, 1946.

Howard, S. L., Erofeeva, S., and Padman, L.: CATS2008: Circum-Antarctic Tidal Simulation version 2008, https://doi.org/10.15784/601235, 2019.

Huilgol, R.: On the concept of the Deborah number, Transactions of the Society of Rheology, 19, 297–306, 1975.

Huth, A., Adcroft, A., and Sergienko, O.: Parameterizing Tabular-Iceberg Decay in an Ocean Model, Journal of Advances in Modeling Earth Systems, 14, e2021MS002 869, 2022.

James, T. D., Murray, T., Selmes, N., Scharrer, K., and O'Leary, M.: Buoyant flexure and basal crevassing in dynamic mass loss at Helheim Glacier, Nature Geoscience, 7, 593–596, 2014.

Jenkins, A.: Convection-driven melting near the grounding lines of ice shelves and tidewater glaciers, Journal of Physical Oceanography, 41, 2279–2294, 2011.

Jenkins, A., Corr, H. F., Nicholls, K. W., Stewart, C. L., and Doake, C. S.: Interactions between ice and ocean observed with phase-sensitive radar near an Antarctic ice-shelf grounding line, Journal of Glaciology, 52, 325–346, 2006.

Jeong, H., Asay-Davis, X. S., Turner, A. K., Comeau, D. S., Price, S. F., Abernathey, R. P., Veneziani, M., Petersen, M. R., Hoffman, M. J., Mazloff, M. R., and Ringler, T. D.: Impacts of ice-shelf melting on water-mass transformation in the Southern Ocean from E3SM simulations, Journal of Climate, 33, 5787 – 5807, https://doi.org/10.1175/JCLI-D-19-0683.1, 2020.

Klein, E., Mosbeux, C., Bromirski, P. D., Padman, L., Bock, Y., Springer, S. R., and Fricker, H. A.: Annual cycle in flow of Ross Ice Shelf, Antarctica: Contribution of variable basal melting, Journal of Glaciology, 66, 861–875, 2020.

Li, Q., England, M. H., Hogg, A. M., Rintoul, S. R., and Morrison, A. K.: Abyssal ocean overturning slowdown and warming driven by Antarctic meltwater, Nature, 615, 841–847, 2023.

Mansfield, E.: Chapter I - Derivation of the basic equations, in: The Bending and Stretching of Plates, vol. 6 of *International Series of Monographs on Aeronautics and Astronautics: Solid and Structural Mechanics*, pp. 3–20, Pergamon, ISBN 978-1-4831-9763-0, https://doi.org/https://doi.org/10.1016/B978-1-4831-9763-0.50007-0, 1964.

Martin, T. and Adcroft, A.: Parameterizing the fresh-water flux from land ice to ocean with interactive icebergs in a coupled climate model, Ocean Modelling, 34, 111–124, 2010.

Meier, W. N., Fetterer, F., Windnagel, A. K., and Stewart, J. S.: NOAA/NSIDC Climate Data Record of Passive Microwave Sea Ice Concentration, Version 4, https://doi.org/10.7265/efmz-2t65, 2021.

Mosbeux, C., Wagner, T. J. W., Becker, M. K., and Fricker, H. A.: Viscous and elastic buoyancy stresses as drivers of ice-shelf calving, Journal of Glaciology, 66, 643–657, 2020.

Mosbeux, C., Padman, L., Klein, E., Bromirski, P. D., and Fricker, H. A.: Seasonal variability in Antarctic ice shelf velocities forced by sea surface height variations, The Cryosphere, 17, 2585–2606, 2023.

NASA/JPL: GHRSST Level 4 MUR global foundation sea surface temperature analysis (v4.1), https://doi.org/10.5067/GHGMR-4FJ04, 2015.

Padman, L., King, M., Goring, D., Corr, H., and Coleman, R.: Ice-shelf elevation changes due to atmospheric pressure variations, Journal of Glaciology, 49, 521–526, 2003.

https://doi.org/10.5194/egusphere-2024-571
Preprint. Discussion started: 26 March 2024

Padman, L., Erofeeva, S. Y., and Fricker, H. A.: Improving Antarctic tide models by assimilation of ICESat laser altimetry over ice shelves, Geophysical Research Letters, 35, 2008.

Pattyn, F. and Morlighem, M.: The uncertain future of the Antarctic Ice Sheet, Science, 367, 1331–1335, 2020.

Reeh, N.: On the calving of ice from floating glaciers and ice shelves, Journal of Glaciology, 7, 215–232, 1968.

Rignot, E., Jacobs, S., Mouginot, J., and Scheuchl, B.: Ice-shelf melting around Antarctica, Science, 341, 266–270, https://doi.org/10.1126/science.1235798, 2013.

Sayag, R. and Worster, M. G.: Elastic dynamics and tidal migration of grounding lines modify subglacial lubrication and melting, Geophysical Research Letters, 40, 5877–5881, 2013.

Scambos, T., Sergienko, O., Sargent, A., MacAyeal, D., and Fastook, J.: ICESat profiles of tabular iceberg margins and iceberg breakup at low latitudes, Geophysical Research Letters, 32, 2005.

Schmidt, G. A., Romanou, A., Roach, L. A., Mankoff, K. D., Li, Q., Rye, C. D., Kelley, M., Marshall, J. C., and Busecke, J. J.: Anomalous meltwater from ice sheets and ice shelves is a historical forcing, Geophysical Research Letters, 50, e2023GL106 530, 2023.

Seroussi, H., Nowicki, S., Payne, A. J., Goelzer, H., Lipscomb, W. H., Abe-Ouchi, A., Agosta, C., Albrecht, T., Asay-Davis, X., Barthel, A., et al.: ISMIP6 Antarctica: a multi-model ensemble of the Antarctic ice sheet evolution over the 21st century, The Cryosphere, 14, 3033–3070, 2020.

Shuman, C. A., Zwally, H. J., Schutz, B. E., Brenner, A. C., DiMarzio, J. P., Suchdeo, V., and Fricker, H. A.: ICESat Antarctic elevation data: Preliminary precision and accuracy assessment, Geophysical Research Letters, 33, 2006.

Slater, D., Benn, D., Cowton, T., Bassis, J., and Todd, J.: Calving multiplier effect controlled by melt undercut geometry, Journal of Geophysical Research: Earth Surface, 126, e2021JF006 191, 2021.

Slater, D. A., Straneo, F., Das, S. B., Richards, C. G., Wagner, T. J. W., and Nienow, P. W.: Localized plumes drive front-wide ocean melting of a Greenlandic tidewater glacier, Geophysical Research Letters, 45, 12–350, 2018.

Stewart, C. L., Christoffersen, P., Nicholls, K. W., Williams, M. J., and Dowdeswell, J. A.: Basal melting of Ross Ice Shelf from solar heat absorption in an ice-front polynya, Nature Geoscience, 12, 435–440, 2019.

Sutherland, D., Jackson, R. H., Kienholz, C., Amundson, J. M., Dryer, W., Duncan, D., Eidam, E., Motyka, R., and Nash, J.: Direct observations of submarine melt and subsurface geometry at a tidewater glacier, Science, 365, 369–374, 2019.

Trevers, M., Payne, A. J., Cornford, S. L., and Moon, T.: Buoyant forces promote tidewater glacier iceberg calving through large basal stress concentrations, The Cryosphere, 13, 1877–1887, 2019.

Vaughan, D. G.: Tidal flexure at ice shelf margins, Journal of Geophysical Research: Solid Earth, 100, 6213–6224, 1995.

Vella, D. and Wettlaufer, J.: Explaining the patterns formed by ice floe interactions, Journal of Geophysical Research: Oceans, 113, 2008.

Wagner, T. J. W. and Eisenman, I.: How climate model biases skew the distribution of iceberg meltwater, Geophysical Research Letters, 44, 3691–3699, 2017.

Wagner, T. J. W., Wadhams, P., Bates, R., Elosegui, P., Stern, A., Vella, D., Abrahamsen, E. P., Crawford, A., and Nicholls, K. W.: The "footloose" mechanism: Iceberg decay from hydrostatic stresses, Geophysical Research Letters, 41, 5522–5529, 2014.

Wagner, T. J. W., James, T. D., Murray, T., and Vella, D.: On the role of buoyant flexure in glacier calving, Geophysical Research Letters, 43, 232–240A, 2016.

White, F. M., Spaulding, M. L., and Gominho, L.: Theoretical Estimates of the Various Mechanisms Involved in Iceberg Deterioration in the Open Ocean Environment., Rhode Island University, Kingston, 1980.

https://doi.org/10.5194/egusphere-2024-571
Preprint. Discussion started: 26 March 2024

Zwally, H. J., Schutz, R., Hancock, D., and Dimarzio, J.: GLAS/ICESat L2 Global Antarctic and Greenland Ice Sheet Altimetry Data (HDF5), Version 34, https://doi.org/10.5067/ICESAT/GLAS/DATA209, 2014.